Applied Clay Science 163 (2018) 164–177

Contents lists available at ScienceDirect

Applied Clay Science

journal homepage: www.elsevier.com/locate/clay

Research paper

A molecular dynamics framework to explore the structure and dynamics of layered double hydroxides

Germán Pérez-Sánchez[a,*], Tiago L.P. Galvão[b], João Tedim[b], José R.B. Gomes[a]

[a] CICECO – Aveiro Institute of Materials, Department of Chemistry, University of Aveiro, Campus Universitário de Santiago, P-3810-193 Aveiro, Portugal
[b] CICECO – Aveiro Institute of Materials, Department of Materials and Ceramic Engineering, University of Aveiro, Campus Universitário de Santiago, P-3810-193 Aveiro, Portugal

ARTICLE INFO

Keywords:
Density functional theory
Molecular dynamics
Force field
CLAYFF
LDH

ABSTRACT

It is presented a straightforward procedure based on the CLAYFF force field to perform molecular dynamics (MD) computer simulations with the GROMACS open source package of layered double hydroxide (LDH) materials with different intercalated anions. This procedure enables running very long simulations of systems where all atomic positions are allowed to move freely, while maintaining the integrity of the LDH structure intact. Therefore, it has the potential to model different important applications of LDH involving ion-exchange and interlayer equilibrium processes in diverse areas as drug delivery, water purification, and corrosion protection. The magnesium-aluminium based LDH with a metallic ratio 2:1 (Mg_2Al) was chosen to validate our computer simulation framework, because of the comprehensive experimental and computational studies reported in the literature devoted to the understanding of the structure of Mg_2Al LDH. Potential parameters from the literature were used to model the Mg_2Al LDH with different intercalated anions using a new set of atomic point charges calculated with the DDEC6 formalism. Once the model was validated through careful comparisons of the simulated and experimental structures, the procedure was adapted to the Zn_2Al LDH materials. Lennard-Jones parameters had to be developed for zinc (II) cations and calibrated using the experimental structural data found in the literature for Zn_2Al LDH and the height of the galleries determined experimentally in this work for Zn_2Al with intercalated nitrate anions. The consistency of the model is proved by carrying out MD simulations to reproduce in the computer the typical experimental conditions in which the Zn_2Al LDH is immersed in a sodium chloride water solution to act as a nanotrap for aggressive anions in corrosion protection applications. The LDH structure is maintained in the MD simulation in which the LDH is free to move alongside the solution and allowing a natural anion exchange between the LDH and the solution as well as dehydration/hydration of the basal space.

1. Introduction

Layered double hydroxides (LDH) are known as smart macromolecular containers with bifunctional capacity (Richetta et al., 2017). They are capable of hosting functional molecules and release them upon demand, whilst retrieving target species. LDH are constituted by mixed metal cation hydroxide layers held together by interlayers composed of charge compensating anions and water. The interlayers are dominated by electrostatic interactions and complex hydrogen bonding networks. The most widely studied LDH materials have the general formula $[M^{2+}_{1-x}M^{3+}_{x}(OH)_2]^{x+}(A^{n-})_{x/n}mH_2O$, where M^{2+} and M^{3+} are di- and trivalent cations present in a molar ratio (x) obtained as $M^{3+}/(M^{2+} + M^{3+})$, and A^{n-} is the anion. Singly (M^{+}) and quadruple (M^{4+}) charged cations such as Li^{+} and Ti^{4+} or Zr^{4+} can also be incorporated in the mixed metal cation hydroxide layers. In the present study, M^{2+} is Mg^{2+} or Zn^{2+}, and M^{3+} is Al^{3+}, with a molar ratio of 2:1 of M^{2+} to M^{3+} ($x = 0.33$). The anions considered are Cl^{-}, NO_3^{-} or CO_3^{2-} either solvated with one or two water molecules (m = 1,2). Depending on the nature of the anions, LDH can be relevant materials with commercial interest to be explored in catalysis, (Lu et al., 2016a) adsorption, (Lu et al., 2016b; Yan et al., 2016) drug delivery (Li et al., 2016; Senapati et al., 2016) or water purification (Yokoi et al., 2016).

The anion-exchange ability of LDH allows them to act as reservoirs for functional anions. The latter can be released upon an external trigger, e.g. a targeted species from the surroundings, which can be temporarily or permanently retrieved by releasing more labile ones. One application in which this property of LDH assumes a fundamental role is in corrosion protection. LDH are able to entrap corrosive species,

* Corresponding author at: Campus Universitário de Santiago, University of Aveiro, Aveiro, Portugal.
E-mail address: gperez@ua.pt (G. Pérez-Sánchez).

https://doi.org/10.1016/j.clay.2018.06.037
Received 14 April 2018; Received in revised form 15 June 2018; Accepted 25 June 2018
Available online 21 July 2018

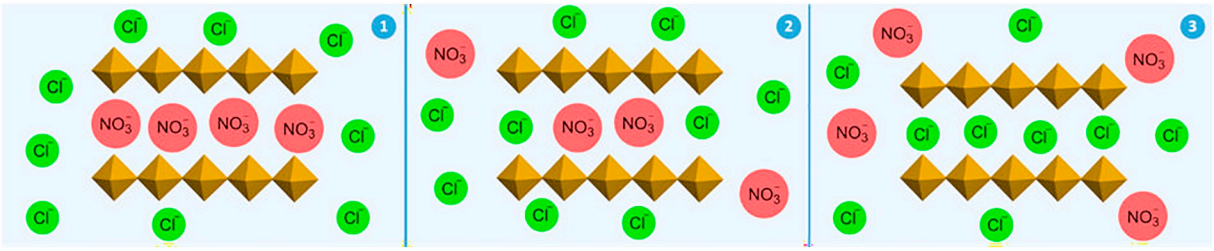

Fig. 1. Scheme with the release of nitrate and intercalation of chloride in the LDH interlayer structure. Green/red circles and yellow polyhedra represent, chloride/nitrate anions and the LDH metal hydroxide layers, respectively. (For interpretation of the references to colour in this figure legend, the reader is referred to the web version of this article.)

such as chlorides, (Tedim et al., 2012) and to respond to aggressive electrolyte conditions (Zheludkevich et al., 2012). These layered materials are then ideal macromolecular containers that can be incorporated as additives in functional coatings (Serdechnova et al., 2016), or that can form nanostructured conversion films on top of metallic alloys (Tedim et al., 2011).

Tedim et al. (Tedim et al., 2012) demonstrated that when dispersed in a polymeric coating commonly used in the automotive industry for corrosion protection, zinc-aluminium LDH, with a metallic ratio of 2:1 and intercalated nitrate anions (Zn_2Al-NO_3 LDH), can decrease the permeability of the coatings to chlorides in solution. The choice of the nitrate anion was based on its lower affinity to the LDH interlayers when compared to that of the chloride anion (Miyata, 1983; Israëli et al., 2000). Due to this differential affinity, chloride anions in solution enter the LDH interlayer distance (the so-called galleries or basal space) and replace the nitrate species. As it is schematically illustrated in Fig. 1, when the Zn_2Al-NO_3 LDH material is in contact with a corrosive chloride solution Fig. 1 panel 1, the lower affinity of NO_3^- anions to stay in the galleries when compared with that displayed by Cl^- anions, promotes their exchange Fig. 1 panel 2 until all the nitrate species are displaced from the galleries Fig. 1 panel 3. The ion-exchange equilibrium between trapping chlorides and releasing nitrates was proved experimentally, (Tedim et al., 2012) and Zn_2Al-NO_3 LDH were suggested as concentration responsive materials.

In the present study, a framework is developed to carry out molecular dynamics (MD) simulations with the aim to analyse the mechanism associated with the equilibrium and to establish the baseline for future ion-exchange studies. The computational work was performed for zinc-aluminium and magnesium-aluminium LDH, with a metallic ratio of 2:1 (zinc/magnesium:aluminium), and with solvated nitrate, chloride or carbonate anions intercalated between the metal hydroxide. The magnesium based LDH was chosen to benchmark the quality of the simulation framework here presented against the information available from the noticeable number of computational and experimental studies found in the literature for this system (Lombardo et al., 2005; Cunha et al., 2016; Wang et al., 2009; Galvão et al., 2016; 2017; Costa et al., 2010; Radha et al., 2007). Then, a similar simulation protocol was extended to the zinc-aluminium LDH materials with the same intercalated anions.

Computer simulations in these materials have been a matter of great interest (Rad et al., 2016; Tsukanov and Psakhie, 2016). However, the studies reported in literature were developed following different approaches, based on diverse Lennard-Jones (LJ) parameters, partial charges and software, thus a unique computational protocol that can be extended to different LDH materials incorporating different anions is still lacking. Importantly, as far as we know, none of the previous computational models are able to reproduce the archetypical experimental conditions where the LDH immersed in solution as nanocontainers of corrosion inhibitors (Tedim et al., 2012; Zheludkevich et al., 2012; Serdechnova et al., 2016; Tedim et al., 2011; Galvão et al., 2016; Poznyak et al., 2009).

Herewith, we are reporting a model that takes into account the periodic expansion of the LDH structure in the directions parallel and perpendicular to the cationic layers with different anions inside the galleries (Thyveetil et al., 2008; Makaremi et al., 2015; Lv et al., 2012). Based on the very satisfactory comparison of calculated and experimental data, it is expected that the model will serve for applications in a wide range of fields, having the potential to predict the controlled release of functional anions, such as corrosion inhibitors (Poznyak et al., 2009) or pharmaceuticals, (Senapati et al., 2016) the trapping of undesired anions (Lu et al., 2016b) or to simulate the influence of pH or other electrolytes (Carneiro et al., 2015). As a test case, the Zn_2Al LDH with intercalated nitrate anions was introduced into a sodium chloride water solution. Encouragingly, it was found that the layered structure of the LDH was not destroyed within the time of a long MD simulation, providing the closest way so far to study an ion or water exchange between the LDH and the solution.

2. Computational methods

2.1. Periodic structures

The LDH crystallographic structure corresponds to the *R-3c* space group. For structures with zinc/aluminium cationic layers, the supercells were described by two lattice parameters, *a* and *c*, that were used to define the vectors of the supercell according to: $\vec{v}_x(2\sqrt{3}a, 0, 0)$, $\vec{v}_y\left(-\sqrt{3}a/2, 3a/2, 0\right)$ and $\vec{v}_z\left(a/2, \sqrt{3}a/2, c/3\right)$.(Costa et al., 2010; Radha et al., 2007; Costa et al., 2012). The lattice parameter *a* is defined by the size and ratio of metal cations in the LDH cationic layers. This parameter was obtained in a previous work (Wang et al., 2009) from the position of the (110) reflection of the powder X-ray diffraction (XRD) pattern. In the case of magnesium/aluminium LDH, the atomic coordinates and lattice parameters of the cationic layer were those described in literature for a natural occurring magnesium/aluminium LDH (Krivovichev et al., 2010) and were taken directly from the powder diffraction file (PDF)-4+ 2016 database of the International Center for Diffraction Data (ICDD). The *c* lattice parameter depends on the interlayer distance occupied by the anions and was taken from literature (Lombardo et al., 2005; Cunha et al., 2016; Wang et al., 2009; Galvão et al., 2016; 2017; Costa et al., 2010; Radha et al., 2007).

Both magnesium/aluminium and zinc/aluminium LDH models with nitrate, chloride, and carbonate anions were built within the supercell approach for periodic repetition in the three dimensions, i.e., Mg_2Al-Cl, Mg_2Al-NO_3, and Mg_2Al-CO_3 or Zn_2Al-Cl, Zn_2Al-NO_3, and Zn_2Al-CO_3 LDH, which are named from now on MI, MII, and MIII or ZI, ZII, and ZIII, respectively. The systems, the supercells and notations used in this work are summarized in Table 1, while Fig. 2 displays the corresponding structural representations. In the present work, the number of water molecules per charge was fixed to the ratio 2:1, which yields two water molecules per chloride or nitrate anion and four water molecules per carbonate species (Table 1). The number of solvating water molecules per anion was chosen according to experimental results presented in literature (Lombardo et al., 2005; Cunha et al., 2016; Ay et al., 2009; Latterini et al., 2007). It should be noted at this point that in the case of

Table 1
Supercells and notations for the LDH systems studied in this work.

LDH System	Supercell	Notation
Mg_2Al-Cl	$[Mg_4Al_2(OH)_{12}]Cl_2{\cdot}4H_2O$	MI[a]
Mg_2Al-NO_3	$[Mg_4Al_2(OH)_{12}](NO_3)_2{\cdot}4H_2O$	MII
Mg_2Al-CO_3	$[Mg_4Al_2(OH)_{12}](CO_3){\cdot}4H_2O$	MIII
Zn_2Al-Cl	$[Zn_4Al_2(OH)_{12}]Cl_2{\cdot}4H_2O$	ZI[a]
Zn_2Al-NO_3	$[Zn_4Al_2(OH)_{12}](NO_3)_2{\cdot}4H_2O$	ZII
Zn_2Al-CO_3	$[Zn_4Al_2(OH)_{12}](CO_3){\cdot}4H_2O$	ZIII

[a] Comparative simulations were performed for the MI and ZI systems but with half of the water molecules, i.e., the supercells $[Mg_4Al_2(OH)_{12}]Cl_2{\cdot}2H_2O$ and $[Zn_4Al_2(OH)_{12}]Cl_2{\cdot}2H_2O$ which are denoted $MI_{1/2}$ and $ZI_{1/2}$, respectively.

magnesium/aluminium and zinc/aluminium LDH with intercalated chloride anions, there are experimental results supporting both one and two water molecules solvating each anion (Lombardo et al., 2005; Cunha et al., 2016). This matter will also be addressed in the present work. Therefore, calculations employing models with one water molecule per anion, cf. $MI_{1/2}$ and $ZI_{1/2}$ (Table 1), respectively, were also performed.

The supercells shown in Fig. 2 were used for the electronic density functional theory (DFT) calculations where all the atomic positions were optimized as it will be detailed below. From the DFT optimized supercells, containing between 38 and 50 atoms depending on the system, systems composed by thousands of atoms (9500–12,500) were built for further classical molecular dynamics (MD) simulations. These large systems resulted from the expansion of the smaller supercells by $5 \times 10 \times 5$ repetitions in the case of NO_3^- and Cl^- intercalated species, and $10 \times 5 \times 5$ in the case of the divalent CO_3^{2-} anion. The quite large supercells were chosen for avoiding any fictitious finite size effects that may hamper, for instance, the possible undulations of the cationic layers suggested to occur in previous studies by other authors (Thyveetil et al., 2007).

2.2. DFT calculations

The atomic positions of the smaller supercells (see Fig. 2) were relaxed by means of periodic model electronic DFT calculations performed with the Quantum ESPRESSO (QE) computer code (Giannozzi et al., 2009) and the Perdew-Burke-Ernzerhof (PBE) (Perdew et al., 1996) exchange-correlation functional, using a methodology found to be very appropriate for these materials (Galvão et al., 2016; Costa et al., 2010; Maruyama et al., 2016). The nuclei and core electrons were described by ultrasoft pseudopotentials (Vanderbilt, 1990) available for the PBE functional in the QE website (http://www.quantum-espresso.org/pseudopotentials/), and the Kohn − Sham orbitals were expanded using plane wave basis sets with 60 Ry cutoff for the kinetic energy and 600 Ry cutoff for the charge density. The first Brillouin Zone integrations were performed with the gaussian smearing method (Marzari et al., 1999) using a smearing parameter of 0.02 and a $2 \times 2 \times 1$ k-point mesh (Monkhorst and Pack, 1976). The relaxation of the atomic positions with fixed lattice parameters were stopped after the forces acting on all atoms in each structure was lower than 10^{-3} Ry/a.u.. The optimized unit cell parameters are provided in Table S1 of the Supplementary Information (SI).

The LDH atomic charges included in CLAYFF (Cygan et al., 2004) were used in preliminary MD simulations where, despite different energy minimization/equilibration protocol attempts, the LDH structures were found to be very unstable, i.e., it was observed significant dissolution of the metal ions from the metal layers into the interlayer water/anion galleries. This issue was also reported in previous studies (Lombardo et al., 2005; Kim et al., 2007; 2005). Therefore, we decided to compute new atomic charges within the density derived electrostatic and chemical (DDEC6) formalism using the Chargemol program, (Manz and Limas, 2016; Limas and Manz, 2016) with charge densities generated with the VASP code (Kresse and Hafner, 1993; Kresse and Furthmüller, 1996a; 1996b). In the latter calculations, the structures optimized with the QE code were recalculated with the PBE functional, but employing projected-augmented wave potentials, (Kresse and Joubert, 1999) 450 eV cutoff for the kinetic energy of the plane waves,

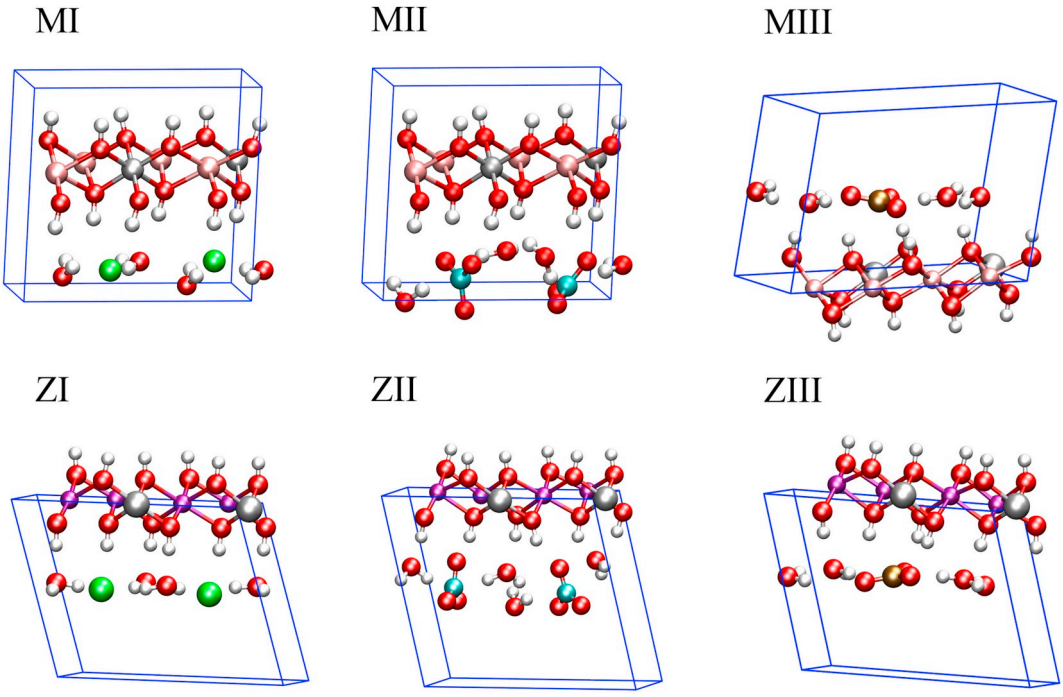

Fig. 2. DFT optimized structures for the MI-MIII (top row) and ZI-ZIII (bottom row) LDH systems. Colour code for spheres: silver is Al; pink is Mg; purple is Zn; green is Cl; cyan is N; ochre is C; red is O; and white is H. (For interpretation of the references to colour in this figure legend, the reader is referred to the web version of this article.)

Table 2
Partial charges (q, in a. u.) calculated for the magnesium- (MI-MIII) and zinc- (ZI-ZIII) aluminium LDH with nitrate, chloride and carbonate anions.

Atom	q (MI, MII and MIII)	q (ZI, ZII and ZIII)
Mg/Zn	1735	1050
Al	1440	1690
O_{OH}	−1080	−0.930
H_{OH}	0.477	0.465
$N_{nitrate}$	0.860	
$O_{nitrate}$	−0.620	
$C_{carbonate}$	0.931	
$O_{carbonate}$	−0.977	
$Cl_{chloride}$	−1000	
O_{water}	−0.848	
H_{water}	0.424	

$3 \times 3 \times 1$ k-point meshes for the numerical integration in the reciprocal space, and convergence criteria on the total energy change and on the forces acting on the ions of 10^{-5} eV and 10^{-2} eV/Å, respectively. The charges were firstly calculated for the systems MI, MII, and MIII. Despite the presence of different anions, e.g. Cl^-, NO_3^-, and CO_3^{2-}, respectively, the calculated charges for magnesium (Mg), aluminium (Al), hydroxide oxygen (O_{OH}) and hydroxide hydrogen (H_{OH}), presented small differences. Therefore, we decided to use an average value for each of these atomic species. Also, we found that the average of the calculated charges for the H and O atoms in the water molecules were close to the charges in the SPC/E water model (Berendsen et al., 1987). Consequently, our model uses the SPC/E model for the water molecules in the galleries. The calculated charges of the charge balancing anions were slightly lower than −1 a.u. (NO_3^-, Cl^-) or −2 a.u. (CO_3^{2-}). For convenience, we rounded the charges to have a −1 or −2 net charge in all these cases and, consequently, counterbalance the +1 charge of the metal hydroxide layers. The charges obtained for the magnesium-aluminium LDH are compiled in Table 2. A similar protocol was followed to obtain the atomic charges for the zinc-aluminium LDH systems and the charges are also provided in Table 2. As described below, by using the new set of atomic charges, the dissolution of the metal ions in the MD simulations was residual.

2.3. Molecular dynamics simulations

The classical MD simulations were carried out with Gromacs 5.1.4 package (Abraham et al., 2015) using a leapfrog algorithm (Hockney et al., 1974) to integrate the equations of motion, unless otherwise stated, with a time step of 1 fs. The energy contribution terms in the potential energy function were the bond stretching, angle bending, and dihedral torsion, in the case of the interactions between bonded atoms, and the Lennard-Jones (LJ) potential and the Coulomb term in the case of the intermolecular interactions. The energy contributions in the potential energy function, bond stretching, angle bending, and dihedral torsion were taken for bonded interactions whereas the Lennard-Jones (LJ) potential and the Coulomb term were considered to take into account the non-bonded interactions. A potential force-switch modifier function was used in LJ with a cut-off radius of 1.4 nm, where the energy decays smoothly to zero between 0.8 and 1.4 nm. The long-range electrostatic interactions were calculated by a combination of particle mesh Ewald and using a coulomb potential-shift function with a cutoff radius of 1.4 nm.

The temperature was fixed at 298 K with the velocity-rescaling (Bussi et al., 2007) in the equilibrium simulations before the production run with the Nose-Hoover thermostat (Hoover, 1985; Nosé, 1984). The pressure coupling was considered as semi isotropic in XY and Z directions and the pressure was fixed at 1 bar using the Berendsen pressure-coupling method (Berendsen et al., 1984) in the equilibrium steps and the Parrinello − Rahman barostat (Parrinello and Rahman, 1981) in the production runs. Bond lengths were constrained by the LINCS algorithm (Hess et al., 1997).

The LJ parameters for the MD simulations were taken from the literature. The conventional LJ function with the CLAYFF force field (Cygan et al., 2004) parameters were used to take into account the non-bonded interactions in the metal hydroxide layers, with the exception of zinc ions (see below). The SPC/E potential model (Berendsen et al., 1987) was selected for water. The potentials from (Smith and Dang, 1994) (Cadena and Maginn, 2006) and Schmid et al. (Schmid et al., 2011) were used for the Cl^-, NO_3^-, and CO_3^{2-} species respectively. Further details are given in Table S2.

The lack of LJ parameters for zinc atoms in CLAYFF induced to explore different approaches to overcome this limitation. For instance, (Lombardo et al., 2005) derived the following LJ parameters $D_0 = 1.0 \times 10^{-6}$ kcal mol^{-1}, $R_0 = 5.0$ Å and $q = 1.05$ a.u. for zinc(II) from calculations involving the minerals ε-$Zn(OH)_2$, γ-$Zn(OH)_2$, and $Zn_5(OH)_8Cl_2{\cdot}H_2O$, which were then used to model the Zn_2Al-Cl LDH material. Other authors used parameters from the universal force field (UFF) or the Dreiding force field (Rad et al., 2016; Káfuňková et al., 2010). In such studies, the results from the simulations compared very satisfactorily with available experimental structural data. Herewith, the LJ parameters for zinc (II) were developed using those parameters by Lombardo et al. as an initial guess. The parameters were firstly optimized upon comparison of the structures for the ZII system arising from our MD simulations and from our own experimental sample and after upon comparison of the structures of the all the Zn_2Al LDH with literature data.

From the molecular structures prepared as described in Section 2.1, a careful energy minimization and equilibrium protocol has been followed. All systems were initially energy minimized in two steps: firstly, the metal atoms and the hydroxide (OH) groups were constrained at their DFT optimized positions, and only the water molecules and the ions were allowed to move, which was followed by a second minimization step where only the metal atoms were frozen, and the remaining atoms were allowed to move. After the energy minimization steps, two NVT simulations were done to equilibrate the initial temperature, one fixing the metal atoms and the OH groups while freely moving the remaining components of the system (1 ns) and another one constraining only the metal atoms (2.5 ns). These two NVT steps allow the accommodation of the intercalated species occupying all the available basal space to avoid the system being locked in a local energy minimum, which assumes great importance in systems composed by the NO_3^- or CO_3^{2-} anions, where different spatial orientations for these species are possible. The energy minimisation and equilibrium simulations steps were run with a time step of 0.5 fs. The equilibrated systems from the NVT simulations were then used in subsequent NpT simulations that lasted 70 ns without imposing any movement constraints in the atoms. In these simulations, the first 50 ns were used for the density equilibration while the last 20 ns were used for production. The potential energy, temperature, density and total energy were monitored to ensure that equilibrium states were attained at the end of the NVT and NpT equilibration runs.

X-Ray diffraction patterns (XRD) of the MII and ZII experimental samples synthesized in our laboratory were compared with the computed XRD pattern of the MD counterparts to benchmark the quality of the computational model to reproduce the experimental LDH structures.

Density profiles, radial distribution functions and the probability angle distributions were obtained from the last 20 ns of the NpT simulations with the Gromacs *gmx density*, *gmx rdf* and *gmx gangle* tools, respectively.

The structure data analysis tool of the crystal structure visualization package Mercury (Groom et al., 2016) (https://www.ccdc.cam.ac.uk/solutions/csd-system/components/mercury) was used to obtain the XRD pattern of each frame, which are all plotted in the same XRD pattern representation.

The 2θ angle value of the d_{003} peak is used to estimate the interlayer

distance d with the following relation Bragg's law,

$$d = \frac{\lambda}{2 \sin\theta} \quad (1)$$

where λ = 1.54056 Å is the wavelength of the X-Ray source.

3. Experimental section

3.1. Materials

$Zn(NO_3)_2{\cdot}6H_2O$ (99%), $Mg(NO_3)_2{\cdot}6H_2O$ (99%), $Al(NO_3)_3{\cdot}9H_2O$ (98.5%), $NaNO_3$ (99.5%) and NaOH (98%) were obtained from Sigma-Aldrich and used without any further purification.

3.2. Synthesis of layered double hydroxides

Zn_2Al-NO_3 and Mg_2Al-NO_3 LDH were synthesized in this work in order to compare the structural features with those obtained by MD for systems ZII and MII, respectively. Both materials were synthesized using a two-step methodology, involving first the co-precipitation at a nearly constant pH of 9–10, followed by the growth of the particles by hydrothermal treatment. The reaction was carried out under nitrogen atmosphere and all the solutions were prepared using previously boiled and nitrogen saturated distilled water, in order to minimize the amount of carbonate anion present in solution and prevent its intercalation.

During the co-precipitation step, a 50 mL mixture of 0.5 M Zn $(NO_3)_2{\cdot}6H_2O$ or $Mg(NO_3)_2{\cdot}6H_2O$ and 0.25 M $Al(NO_3)_3{\cdot}9H_2O$ was added dropwise to a 100 mL solution of 1.5 M $NaNO_3$, under vigorous stirring at room temperature. During this process, the pH was kept nearly constant by simultaneous addition of 2 M NaOH (~50 mL). Afterwards, the obtained product was subjected to a hydrothermal treatment of 373 K for four hours. In the end, the product was centrifuged and washed 4 times with 25 mL of boiled and nitrogen saturated distilled water per 5 g of obtained slurry. A small fraction of the LDH was then dried at 333 K during 4 h for the XRD measurements.

3.3. Characterization of materials

The powder XRD characterization at room temperature of the obtained Zn_2Al-NO_3 and Mg_2Al-NO_3 LDH was performed using a PANalytical X'Pert Powder diffractometer (Ni filtered Cu Kα radiation, a tube power of 45 kV and 40 mA) coupled with a PIXcell^{1D} detector, and an exposition time of 6 s per step of 0.02° over an angular range (2θ) between 4 and 65°.

4. Results and discussion

The main aim of this work is to provide a computer modelling framework for MD simulations of magnesium-aluminium and zinc-aluminium LDH materials with different anions in the interlayer distances. We seek to have a straightforward and intuitive model in which it is not necessary to deal with different parameters and charges depending on the nature of the intercalated anions. Ultimately, the replacement of one anion by another anion requires only the parametrization of the latter without being needed any modification of the parameters for the metal hydroxide layers or the water molecules. This is an important fact to take into account for anion-exchange studies in LDH materials.

For this purpose, the Mg_2Al LDH with different intercalated anions has been taken as a reference due to the vast amount of data available in the literature. Thereby, a structural characterization analysis has been carefully carried out to compare the LDH structures obtained in the MD simulations with results from previous computational and experimental studies.

Fig. 3 shows the snapshots of the final NpT MD production run configurations for system MI after 20 ns of production run and also the density profiles for the metal atoms, hydroxyl groups, anions and water molecules for two adjacent layers along the direction normal to the metal layers. Fig. 3a gives a picture about how chloride anions were arranged as single and double layers in the basal space yielding a strong bending in the LDH structure. The density profile of two adjacent metal layers is plotted in Fig. 3b and confirms this behaviour with three chloride peaks in green. The central one represents the single layer of chlorides in the middle of the basal space, whereas the two adjacent green peaks correspond to those from the double layer of chlorides which are separated by water (blue peaks). As a consequence of this particular single/double chloride layer arrangement, the MI system depicts two different interlayer distances, which is also reflected by the two metal peaks (black line) in the density profile. Thus, the distance between the two black peaks in one and the opposite side of the chloride/water basal space provides a rough estimation of both interlayer distances, being 7.66 Å and 8.86 Å for the single and double chloride layer configuration, respectively. These results are in reasonable agreement with previous computational studies (Wang et al., 2001) and experiments (Miyata, 1983; Boclair et al., 1999). It must be inferred from these previous studies that the anion/water ratio strongly affects the LDH interlayer arrangement as it will be discussed in detail below.

Fig. 4a and b summarise the behaviour of the MII in which NO_3^- anions predominantly were arranged with their molecular planes in a tilted configuration with respect to the planes of the metal layers. In this case, the intercalated NO_3^- anions can be found in the middle of the basal space, with the nitrogen atoms (cyan line in the density profile of Fig. 4b) equidistant from the metal atoms (black lines in Fig. 4b) in consecutive metal hydroxide layers. The interlayer distance can be approximately estimated by measuring the distance between the two adjacent metal atom peaks (black). An interlayer distance of 8.70 Å was obtained by averaging the five basal distances in the MD supercell which is in good agreement with previous experimental results of 8.79 and 8.89 Å. (Miyata, 1983; Sun et al., 2010) as well as with the value determined from XRD analysis of the experimental sample synthesized in our laboratories.

The symmetry shown by the two dashed red line peaks in both sides of the nitrogen atoms (cyan) means that NO_3^- anions were arranged in a preferred angle with respect to the metal layer. Fig. S1 in the SI shows the angle probability distribution of NO_3^- anions in the MD simulation which fall in a range of 80–100° as it can be inferred by the broad blue peak around 90°. This result is in agreement with experiments (Wang et al., 2009; Wang and Wang, 2007) in which the intercalated NO_3^- organisation strongly depends on the density charge of the layer according to the Mg:Al ratio. Wang et al. found that when the Mg:Al ratio is 2:1, 3:1 or 4:1, the LDH structures accommodate tilted only, a mix of tilted/parallel, and parallel-only NO_3^- species, respectively (Wang et al., 2009).

Fig. 5 shows the behaviour of CO_3^{2-} anions in the MIII system which, contrarily to the NO_3^- anions in the MII system, adopted preferentially a parallel orientation with the respect to the metal layer plane as it can be seen in Fig. 5a.

The density profile shown in Fig. 5b confirms that the CO_3^{2-} anions are arranged with their molecular planes parallel to the planes of the metal layers. The maxima of the carbon atoms (ochre) and carbonate oxygens (red dashed lines) peaks as well as that for the water molecules (blue) appear at the centre of the interlayer distance suggesting the formation of a thin layer in the middle of the basal space. The interlayer distance inferred from the density profile is 7.02 Å, slightly lower than that observed experimentally, 7.64 Å (Miyata, 1983) but similar to that found in a previous computational study by (Kim et al., 2005), 7.08 Å. In the latter study, the CO_3^{2-} parallel conformation was found to be stable even at temperatures as high as 500 K. The snapshot shown in Fig. S2 gives some clues about the results obtained in the MD simulations. It is clear that the water molecules are positioned between CO_3^{2-} anions and have a role in the stabilization of the doubly-charged anion -

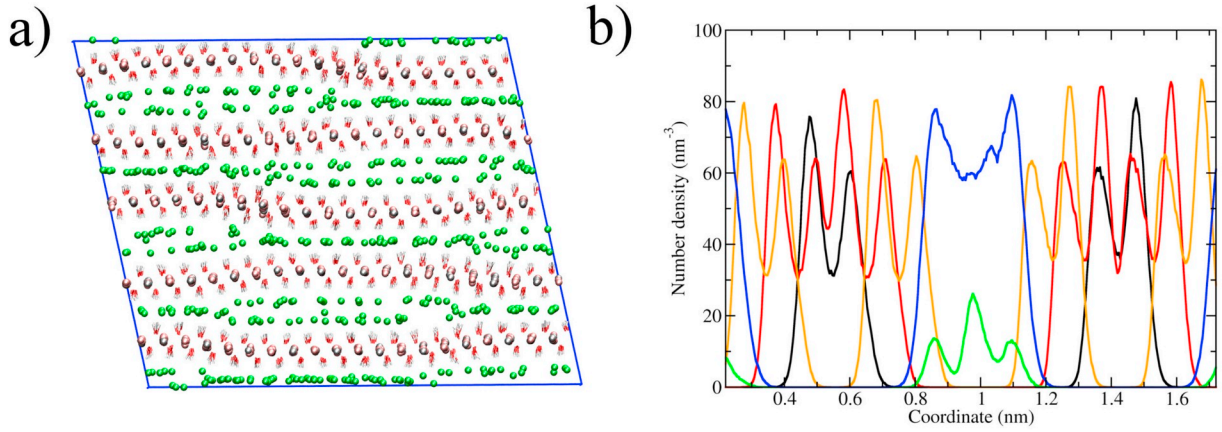

Fig. 3. a) Snapshot with the MI system attained after 20 ns of NpT production run (water molecules were removed for clarity). The colour code is as follows; Magnesium in pink, aluminium in grey, oxygen in red, hydrogen in white and chloride anions in green. b) Density profile obtained along the axis normal to the metal layer with the following colour code: black for metal layer atoms, hydroxide oxygens in solid red lines, hydroxide hydrogens in orange, chloride anions in green and water in blue. (For interpretation of the references to colour in this figure legend, the reader is referred to the web version of this article.)

doubly-charged anion unfavourable interaction. The angle distribution of CO_3^{2-} anions in Fig. S1 shows a peak close to 0° and 180°, with the angle distribution rapidly decreasing up to 20° from the maximum, which suggests that the planar orientation of the CO_3^{2-} species is the most common configuration, also in agreement with the carbonate anion being one of the most thermodynamically favourable anions to be intercalated in LDH (Miyata, 1983; Bravo-Suárez et al., 2004).

It is worth to mention at this point that despite both MII and MIII systems having the same layer density charge (2 Mg:1Al) and number of water molecules per unit of anion charge, the anion arrangement in the basal space was completely different. This antagonistic behaviour is due to the different nature of the intercalated anions, mainly the anion density charge. In the MII system, the anions can move more freely when compared with the MIII system as it can be seen in the simulation films (Supplementary Videos 1 and 2). Since the NO_3^- and the CO_3^{2-} anions have similar sizes, the smaller number of anions and the more important Coulombic interactions with the metal layer in the LDH with carbonate species than with the NO_3^- counterpart, leads to a reduction of the available basal space in MIII when compared with MII. As a consequence, the water molecules (and the anions) have less available space to move, which decreases the degrees of freedom of the water molecules in MIII when compared with MII (cf. sharper peaks for MIII than for MII seen in Fig. S1). It is evident that the CO_3^{2-} anions in the MIII system concentrate more charge per unit volume when compared with the MII system which has two NO_3^- anions per unit cell (Fig. 2). Therefore, CO_3^{2-} anions are trapped in some specific positions being the water molecules constrained between adjacent CO_3^{2-} anions to screen the doubly-charged anion-doubly-charged anion unfavourable interaction as can be seen in the simulation films (Supplementary Videos 2 and 3; in the latter, water molecules were removed for clarity). A detailed picture of the basal conformations of MII and MIII systems is given in Fig. S3a and S3b. The H-bonding distance between anions and the LDH layer was obtained from the first maximum of the RDF profiles for MII (black) and MIII (red) systems showed in Fig. S3c. The H-bonding distance was 1.5 Å in both, thus the difference was mainly the anion orientation. Fig. S3d shows the RDF between the anion oxygen atoms and water molecules in MII and MIII, which can be used to estimate the number of water molecules around the charge compensating anions. In the MII system, more water molecules can be found around the NO_3^- when compared with the first solvation shell of CO_3^{2-} in the MIII system. In the latter, the strong anion/metal layer coulombic interactions push all of the water molecules just between adjacent CO_3^{2-} anions but not among CO_3^{2-} anions and the metal layer as it happens with NO_3^- in MII (see detail in Fig. S3a and S3b).

A stringent test to validate the MI-III structures and, therefore, the force field parameters and the inputs used in the MD simulations can be performed by comparing the computed XRD pattern of the MD cells with their experimental counterparts (Cygan et al., 2009). Thereby, the

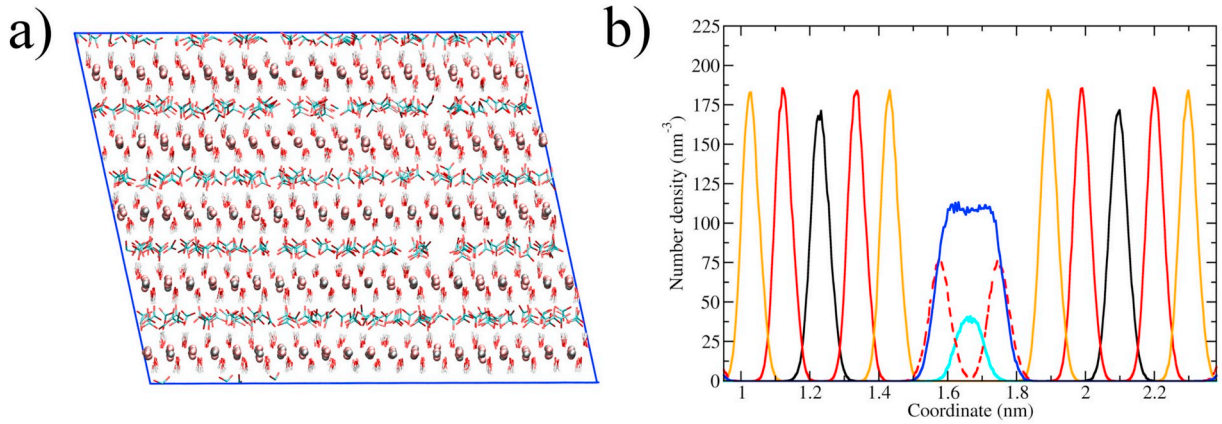

Fig. 4. a) Snapshot with the MII system attained after 20 ns of NpT production run (water molecules were removed for clarity) and the colour code is the same as Fig. 3a but nitrogen in cyan. b) Density profile obtained along the axis normal to the metal layer with the colour code as in Fig. 3b and nitrate nitrogen and oxygen atoms are shown in cyan and red dashed lines, respectively. (For interpretation of the references to colour in this figure legend, the reader is referred to the web version of this article.)

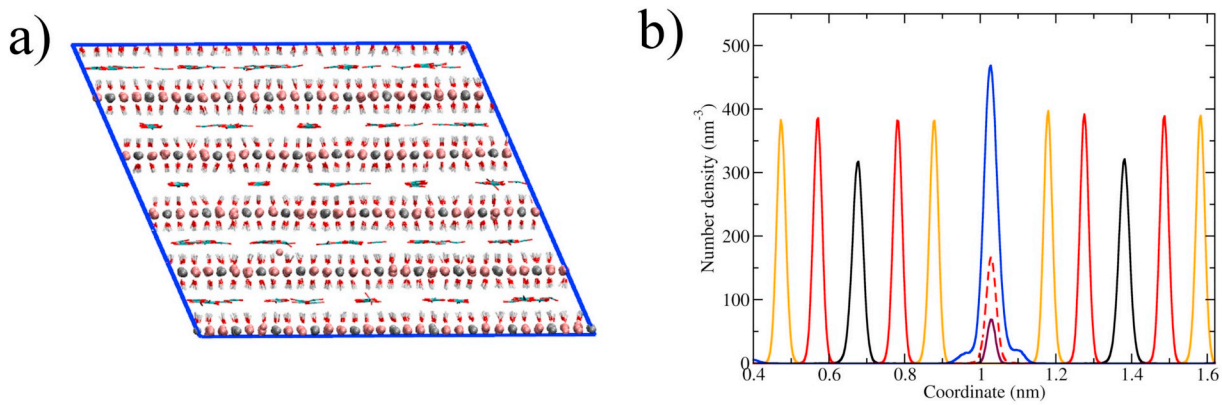

Fig. 5. a) Snapshot with the MIII system attained after 20 ns of simulation time (water molecules were removed for clarity) and the colour code is the same as Fig. 3a but carbon atoms in ochre. b) Density profile obtained along the axis normal to the metal layer with the colour code as in Fig. 3b and carbonate carbon and oxygen atoms in ochre and dashed red, respectively. (For interpretation of the references to colour in this figure legend, the reader is referred to the web version of this article.)

computational XRD pattern has been calculated as follows: 10 frames of the simulation trajectory file, equally distributed in the 20 ns of the production run, were selected (Fig. 6). The small differences found clearly support the convergence of the structures arising from the simulations. Also, the first sharp peak, d_{003}, confirms that all the systems obtained in the MD simulations are highly crystalline.

The XRD pattern for the MI system shown in Fig. 6a displayed an interlayer distance of 8.83 Å, which is in the range of values reported in previous computational studies, 7.23–10.6 Å (Wang et al., 2001), but is larger than the experimental data (Table 3). The chloride arrangement in the MD simulation as single and double layers in the basal space produced the wider XRD d_{003} peak observed in the inset of Fig. 6a and leads to larger uncertainties in the estimation of *d*.

The XRD pattern for the MII system shown in Fig. 6b depicted an interlayer distance of 8.70 Å, which agrees with experiments found in the literature 8.79 Å (Miyata, 1983) and 8.78 Å (Wang et al., 2009). As a further test to validate our MII MD structure, the system was synthesized in our laboratory as described previously and the XRD pattern of the experimental sample was obtained. Fig. S4 shows the comparison between the experimental and the MD XRD patterns, where the d_{003} and d_{006} XRD computational peaks were in satisfactory agreement with the experimental ones, demonstrating that the crystalline structures are similar. Thus, the interlayer distance obtained for the experimental sample was 8.9 Å, in reasonable agreement with the MD counterpart 8.7 Å. It must be noticed that the intensity of the computed XRD profile is lower than the experimental one because of the limited size of the MD sample, as it was previously observed in similar studies (Lombardo et al., 2005). Finally, Fig. 6c shows the XRD pattern for MIII with an interlayer distance of 7.07 Å, lower than the value found in experiments 7.65 Å (Miyata, 1983) but in agreement with previous MD computational studies 7.08 Å (Kim et al., 2005). As a further test, the most relevant interatomic distances were determined from the MD simulations for further comparison with literature data (Table 4).

The structural parameters from the present MD simulations of system MIII are in very good agreement with the results from the Rietveld refinement analysis of the experimental samples (Radha et al., 2007; Bellotto et al., 1996) and of the structure optimized by DFT (Costa et al., 2010). The Mg-O_{OH} and Al-O_{OH} obtained in this work – the (Mg,Al)-O_{OH} value, 2.11 Å, shown in the Table 4 is an averaged Mg-O_{OH} and Al-O_{OH} distance with the aim to compare with literature – are 2.17 Å and 1.99 Å, respectively. Excluding the experimental C—O bond length in carbonate, the experimental and calculated distances are ~0.1 Å and the angles within 2°. The agreement between the present and previous calculated data is even better.

The structural parameters shown in Table 4 for system MIII are compared with those obtained for systems $MI_{1/2}$, MI and MII in Table S3. As it can be seen, the structural parameters for systems MII and MIII are very similar, which suggests that the intercalated species affect only the height of the interlayer galleries and leave almost unchanged the metal hydroxide layers. The fact that other works using different computational steps, e.g. (Wang et al., 2001), yield structures similar to those found in the present study supports our choice of using the same partial charges for all the LDH.

The good agreement between the structures obtained using different computational setups led us to hypothesize that the dissimilarities in the basal distances from the present MD simulations for MI (or MIII) and from the experimental studies might come from different degrees of hydration in the systems studied computationally and experimentally. In fact, previous experimental studied showed that slight differences in the number of water molecules per anion in the basal space can lead to different inter layer distances (Lombardo et al., 2005; Cunha et al., 2016). Bearing this in mind, further studies were performed for the Mg_2Al-Cl LDH with a $1Cl^-$: $1H_2O$ ratio, i.e., the $MI_{1/2}$ system. The MD simulation snapshot in Fig. 7a shows the final structure of $MI_{1/2}$ after 20 ns of production time. It is easily seen that the structure of the $MI_{1/2}$ system is more regular than that described above for the MI system (Fig. 3a). In $MI_{1/2}$, the chloride ions were arranged in a single thin layer and the metal layer bending observed in MI disappeared completely. The density profile in Fig. 7b confirms the homogeneity observed in the simulation snapshot with chloride anions in the middle of the basal space, well surrounded by water molecules.

The computed XRD pattern was used to estimate the interlayer distance following the procedure described above. The result, 7.64 Å, is now much closer to the experimental XRD values of the gallery heights determined by Braterman et al. (Boclair et al., 1999), 7.87 Å and by (Miyata, 1983), 7.86 Å, when compared with the value, 8.83 Å, calculated for the MI system (Table 5).

It is expected that the interlayer distance increases gradually from systems with the $1Cl^-$: $1H_2O$ to the $1Cl^-$: $2H_2O$ ratios. Therefore, the experimental samples studied by Boclair et al. (Boclair et al., 1999) and by (Miyata, 1983) seem to correspond more to systems having a much lower degree of hydration than reported.

The effect of the water content in the basal space is an important aspect to take into account since it strongly affects the stability and homogeneity of the LDH structure as deduced from the comparison of Figs. 3a and 7a. In this regard, (Wang et al., 2001) carried out MD simulations for the Mg_2Al-Cl LDH system with different Cl^-: H_2O ratios using a modified CVFF (Dauber-Osguthorpe et al., 1988) force field, originally designed to model proteins. For systems with $1Cl^-$: $1H_2O$ and $1Cl^-$: $2H_2O$ ratios they found that the chlorides and water molecules were arranged in a thin layer in the middle of the basal space with an interlayer distance of 7.23 Å and ~ 8 Å, respectively, while for a system

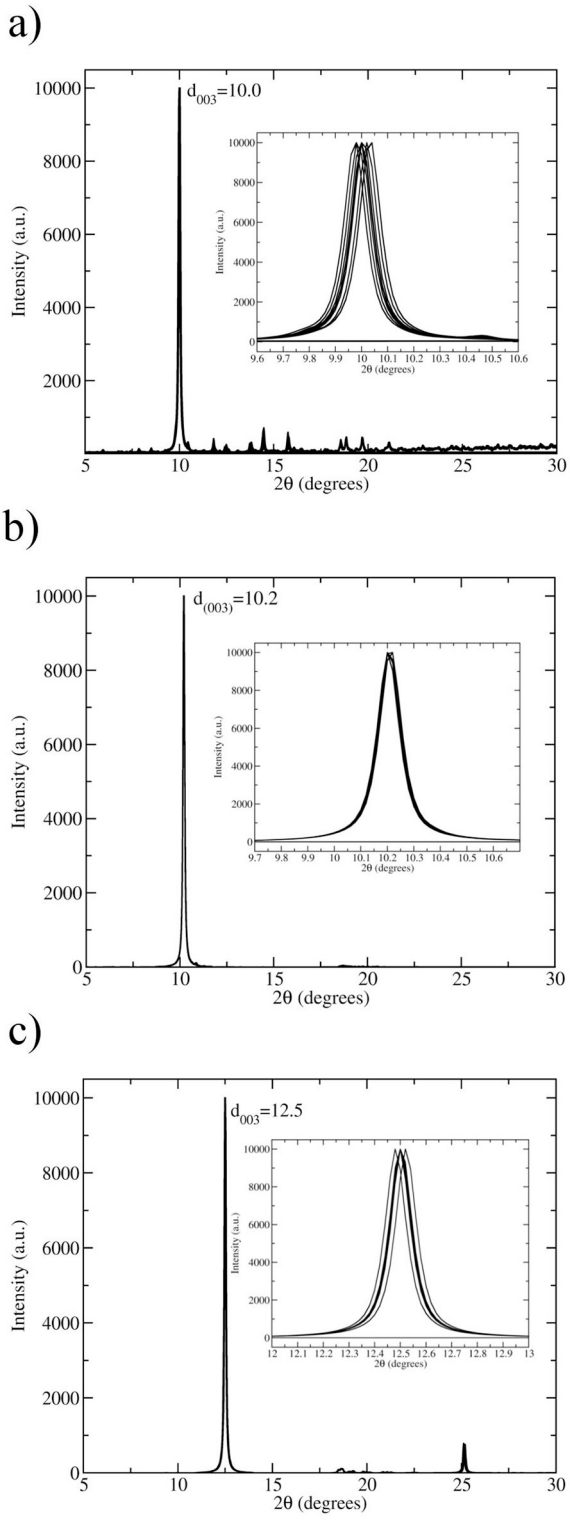

Fig. 6. Computed XRD patterns from the MD simulation runs after 20 ns of production run for systems a) MI, b) MII and c) MII. The 2θ angles given by the d_{003} peaks were used to obtain the interlayer distances shown in Table 3. The inset in all of figures provides a detailed view of the first maximum d_{003}. The MI peak in the inset figure in a) is 0.02 Å wider than those found in MII and MIII mainly due to the single/double chloride layer configuration which introduce more uncertainty in the interlayer distance estimation.

with a ratio ~ $1Cl^-$: $5H_2O$ they reported the formation of a double layer of chlorides and water molecules in the interlayer distance. This confirms that the degree of hydration has an important effect in the gallery space and in the structural integrity of the LDH but, as suggested from the structural results in Table S3, it has a less important effect in the structure of the metal hydroxide layers.

Table 3
Interlayer distance (d) comparison between literature data with those obtained in this work using the computed XRD patterns for MI-III systems shown in Fig. 6. The estimated error in the interlayer distances obtained in this work are lower than 0.01 Å.

System	*d* (Å)			
	This work		Literature	
	MD	Exp.	MD	Exp.
MI	8.83	–	7.23–10.6(Wang et al., 2001)	7.86(Miyata, 1983); 7.87(Boclair et al., 1999)
MII	8.70	8.9	–	8.79(Miyata, 1983); 8.89(Sun et al., 2010)
MIII	7.07	–	7.08 Å(Kim et al., 2005)	7.65(Miyata, 1983)

The MI-III structures obtained in this work are in accordance with previous experiments and computational results, demonstrating the ability of our method to deal with Mg_2Al LDH materials. Thereby, the same approach was applied to Zn_2Al LDH systems. However, the substitution of magnesium by zinc required the calculation of another set of partial charges which are also provided in Table 2. Since LJ parameters for zinc cations are absent in the CLAYFF force field, they had to be parametrized in the present work. We adopted a similar strategy to that used by (Lombardo et al., 2005) in which the D_0 and R_0 values were changed slightly until the simulated structures compared well with available data from the literature for similar systems incorporating zinc cations. In order to obtain our own parameters for zinc, the DFT optimized geometries for the ZI-III unit cells (Fig. 2) were used to prepare the 5 × 10 × 5 and 10 × 5 × 5 supercells for the classical MD simulations. The main interatomic distances from the work of (Lombardo et al., 2005) for the in $ZI_{1/2}$ and ZIII systems were selected as structural references. The best agreement was found with $D_0 = 3.0 \times 10^{-7}$ kcal mol^{-1} and $R_0 = 6.4$ Å (Table S4).

The new parameters for zinc were employed in MD simulations of Zn_2Al LDH systems analogous to the Mg_2Al LDH described above. Fig. 8a shows the results for $ZI_{1/2}$, which presents the chloride ions in the middle of the basal space well arranged in a thin layer mixed with water depicted in the density profile showed in Fig. 8b. When the Cl^-: H_2O ratio is increased to 1:2 resulting in the ZI system, the chlorides anions and the water molecules form a double layer, as it can be seen in Fig. 8c and in the density profile shown in Fig. 8d. Therefore, the effects in the structure of the interlayer upon increasing the Cl^-: H_2O ratio from 1:1 to 1:2 is more dramatic in the case of the Zn_2Al than in the Mg_2Al LDH, where only a mixture of single/double layer conformations was found for MI (Fig. 3a).

The double chloride/water arrangement found in ZI is clearly reflected in the density profile by the two small peaks in the chloride profile in green colour (Fig. 8d). Only a small amount of chloride anions can be found in the middle of the basal space, in contrast to the behaviour observed in $ZI_{1/2}$.

The computed XRD patterns were estimated and interlayer distances of 7.68 and 8.99 Å were obtained for $Z_{1/2}$ and ZI, respectively. These values are compared with data taken from the literature in Table 6. The interlayer distance obtained for $ZI_{1/2}$ agreed with those obtained by XRD, 7.70 Å, (Miyata, 1983) 7.75 Å (Káfuňková et al., 2010) and 7.64 Å, (Velu et al., 1997) and also with 7.69 Å found in the computational studies carried out by (Lombardo et al., 2005) They found in their MD simulations that the $ZI_{1/2}$ system reproduces well the XRD pattern of their experimental samples. The results obtained in their ZI system were in the range of 8.5–8.86 Å (Lombardo et al., 2005; Ennadi et al., 2000; Mahjoubi et al., 2017), which are close to the 8.99 Å obtained in our MD simulations (Fig. 8c and d). It should be remarked that

Table 4
Comparison between the main interatomic distances and angles in our MD MIII structure with literature data.

	This work	Literature	
	MD	MD	Exp.
Interatomic distances (Å)[a]			
(Mg,Al)-O_{OH}	2.11	2.000(Costa et al., 2010)	2.013(1)(Bellotto et al., 1996); 1.991(4)(Radha et al., 2007)
O_{OH}-O_{OH}	2.71	2.569(Costa et al., 2010)	2.632(3)(Bellotto et al., 1996); 2.569(9)(Radha et al., 2007)
C-$O_{carbonate}$	1.31	1.298(Costa et al., 2010)	1.20(4)(Bellotto et al., 1996); 1.098(11)(Radha et al., 2007)
Angles (°)			
O_{OH}-Al,Mg-O_{OH} (inter)	81.0	80.3(Costa et al., 2010)	81.67(6)(Bellotto et al., 1996); 80.4(4)(Radha et al., 2007)
O_{OH}-Al,Mg-O_{OH} (intra)	98.0	–	98.33(6)(Bellotto et al., 1996); 99.64(17)(Radha et al., 2007)
$O_{carbonate}$-C-$O_{carbonate}$	120.1	120(Costa et al., 2010)	120(Bellotto et al., 1996); 120.0(9)(Radha et al., 2007)

[a] Inter and intra between brackets means hydroxyl oxygens placed in the same or adjacent hydroxyl layers, respectively.

a good agreement was found despite different non-bonded parameters for zinc cations and partial charges are used. Another important aspect to take into account is that the supercell size in our system was 50 times larger and the production run was one order of magnitude longer than those considered by Lombardo et al.

The experimental interlayer distance reported by (Ennadi et al., 2000) for the ZI system (cf., 7.83 Å) is much closer to the calculated and experimental values for $ZI_{1/2}$, which suggests they have very probably overestimated the degree of hydration of their sample.

The MD results for the ZII system are shown in Fig. 9a. As in the case of the MII system, the molecular plane of the NO_3^- anions is not coplanar with the metal hydroxide layers. The density profile shown in Fig. 9b shows two clear peaks corresponding to the nitrate oxygen atoms (red dashed lines) which are intermediated by a peak corresponding to the nitrogen atom of nitrate (cyan line). The computed XRD pattern of this system shows an interlayer distance of 8.70 Å, in good agreement with many experimental results found in the literature[71] and with the value (8.80 Å) obtained from the XRD pattern of the experimental sample synthesized in our laboratory (Table 6). Fig. S6 shows the XRD patterns of our experimental sample and of the ZII structure from the MD simulations. The two main d_{003} and d_{006} XRD peaks were clearly found in the computational patterns of ZII in the same positions of the experimental XRD pattern corroborating the quality of the structure obtained in the MD simulations.

Fig. 10a and b display the ZIII structure from the MD simulation together with the density profile. The carbonate anions are coplanar with the metal hydroxide layers forming a thin film together with the water molecules. Fig. S7 shows the angle probability distribution of NO_3^- and CO_3^{2-} with respect to the metal layer plane with the nitrates arranged in tilt angles in ZII whereas the carbonate anions most of them

Table 5
Comparison of the interlayer distances *d* from the computed XRD patterns for the $MI_{1/2}$ and MI systems obtained in this work and data from the literature.

System	*d* (Å)		
	This work	Literature	
		MD	Exp.
$MI_{1/2}$	7.64	7.23(Wang et al., 2001)	7.86(Miyata, 1983); 7.87(Boclair et al., 1999)
MI	8.83		

placed in parallel (angles close to 0° and 180° angle distribution) with some arranged at 40 and 140°, yielding a greater interlayer distance compare with the obtained in the MIII system. The arrangement of the NO_3^- and CO_3^{2-} anions in the basal space obtained in the MD simulations can be compared in Supplementary Videos 4 and 5, respectively. The XRD calculated patterns revealed an interlayer distance of 7.76 Å, in good agreement with literature data, 7.0–7.63 Å (Lombardo et al., 2005; Kim et al., 2007; Velu et al., 1997; Mahjoubi et al., 2017) (Table 6).

The results showed in this work demonstrate that the MD approach is able to handle the complexity of LDH structures. The simulation time and the supercells used in our MD simulations were one order of magnitude larger than those used in previous MD studied, demonstrating a remarkable degree of stability (see Figs. S2 and S8 and Supplemetary Videos 1 to 5). Furthermore, our approach reproduced very well the structures from several different experimental studied and helped to attribute the origins of discrepancies to the different degrees of interlayer hydration. Bearing this in mind, a portion of the ZII system

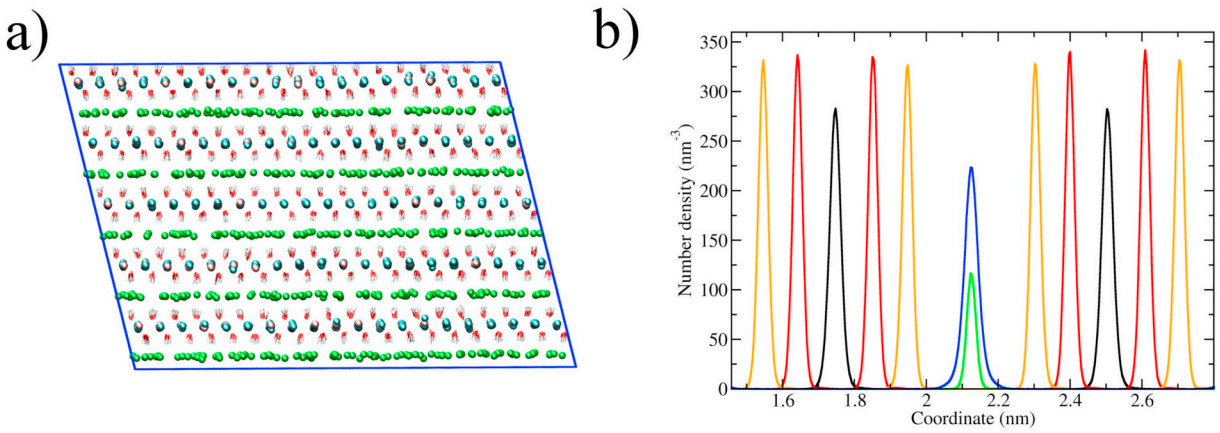

Fig. 7. a) Snapshot with the $MI_{1/2}$ system after 20 ns of production run (water molecules were removed for clarity) and the colour code is the same as Fig. 3a. b) Density profile obtained along the axis normal to the metal layer. (For interpretation of the references to colour in this figure legend, the reader is referred to the web version of this article.)

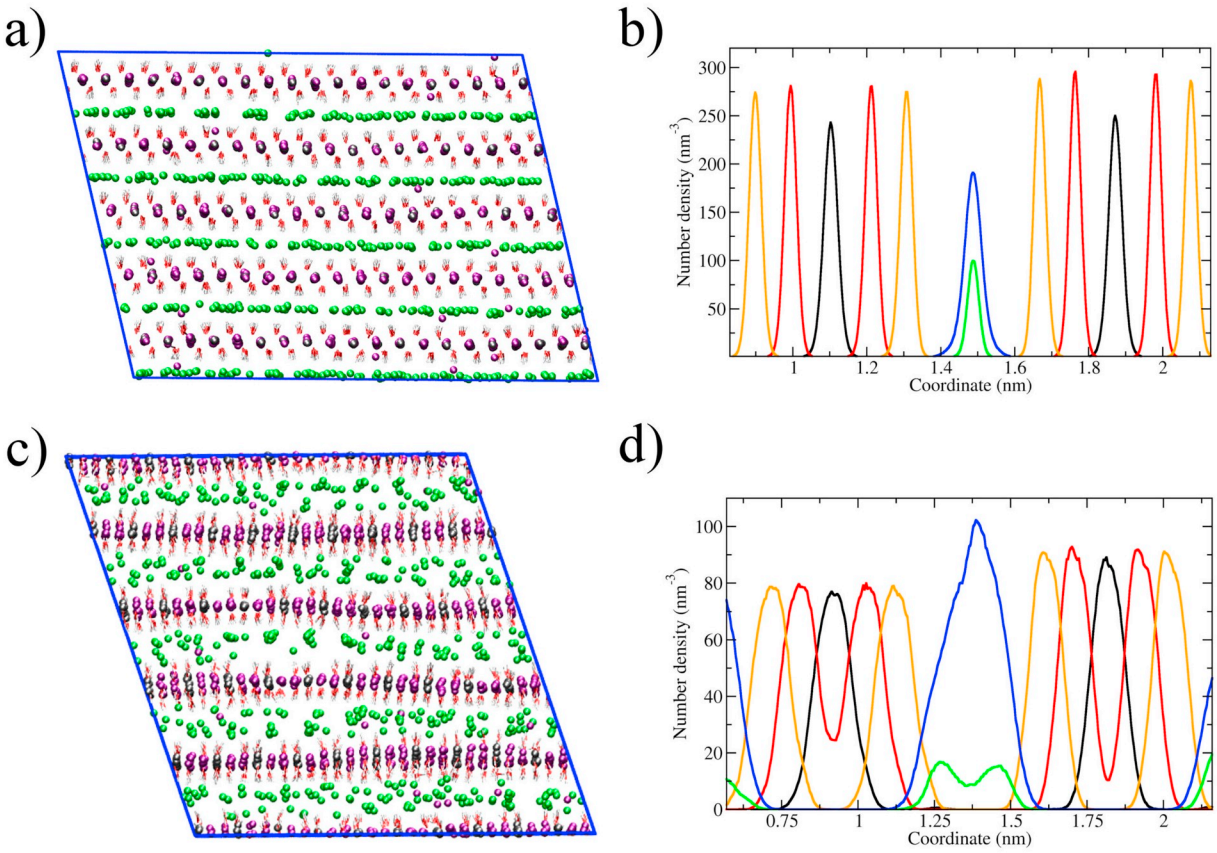

Fig. 8. a) and b) show the simulation snapshot and the density profile for $ZI_{1/2}$, respectively, and c) and d) the same for ZI. The snapshots in a) and c) were taken after 20 ns of simulation time (water molecules were removed for clarity) and the density profiles in c) and d) were obtained along the axis normal to the metal layer. The colour code in a) and c) is as follows; zinc in purple, aluminium in grey, oxygen in red, hydrogen in white and chloride anions in green. (For interpretation of the references to colour in this figure legend, the reader is referred to the web version of this article.)

was put in contact with a sodium chloride water solution in order to explore the feasibility of our model to deal, as close as possible, with usual experimental applications. For instance, (Tedim et al., 2012) showed that the ZII LDH has the ability to capture the Cl^- anions from a corrosive solution upon ion exchange with the NO_3^- placed in the ZII basal space. The addition of ZII to coatings exposed to aggressive environments with chlorides is key for corrosion protection applications. In this direction, the equilibrated ZII system was placed at the centre of a bigger simulation box (12 nm × 12 nm × 12 nm) to which were added 40,000 water and 2000 NaCl molecules. In this new system, the LDH is completely surrounded by the NaCl and water molecules. After the energy minimisation and equilibration steps keeping fixed the atomic positions of the immersed LDH, NpT MD simulation was run for 20 ns. Remarkably, despite periodic molecular repetition restraints are absent in the simulations with the new system, its metal hydroxide structure is maintained and only a very small degree of metal atoms and hydroxyl groups dissolution is seen (Fig. 11a and Supplementary Video 6). This slight dissolution at the top and bottom plane edges of the LDH occurs mainly at the very initial stages of the NpT MD simulation where the positions of the LDH system are now allowed to move freely. We will come to this point at the end of this section. Besides the visual information available in the films (Supporting Information), the stability of the LDH is also well understood from the density profile shown in Fig. 11b. The distance between metal layers (black lines in Fig. 11b) can be used to determine a rough interlayer distance value of 8.94 Å, accordingly with interlayer distance of the material synthesized in our laboratory (8.8 Å). The hydroxyl oxygen and hydrogen curves are overlapping the metal maximum in black and therefore, the immersed ZII system shows a certain degree of bending as it can be seen in Fig. 11a. It must be noticed that this approach will allow the ZII to

Table 6
Comparison between the interlayer distance *d* obtained in this work from the computed XRD patterns of ZI-III and data from the literature.

System	*d* (Å)			
	This work		Literature	
	MD	Exp.	MD	Exp.
$ZI_{1/2}$	7.68	–	7.69(Lombardo et al., 2005)	7.76(Israëli et al., 2000); 7.76–7.83(Lombardo et al., 2005); 7.75(Káfuňková et al., 2010); 7.64(Velu et al., 1997)
ZI	8.99	–	8.5–8.75(Lombardo et al., 2005)	7.83(Ennadi et al., 2000); 8.86(Mahjoubi et al., 2017)
ZII	8.70	8.80	–	8.66(Israëli et al., 2000); 8.73(Rad et al., 2016); 8.53(Velu et al., 1997); 8.84(Mahjoubi et al., 2017); 8.92(Sun et al., 2010)
ZIII	7.76	–	7.50(Lombardo et al., 2005); 7.08(Kim et al., 2005)	7.55–7.63(Lombardo et al., 2005); 7.38(Velu et al., 1997); 7.57(Mahjoubi et al., 2017)

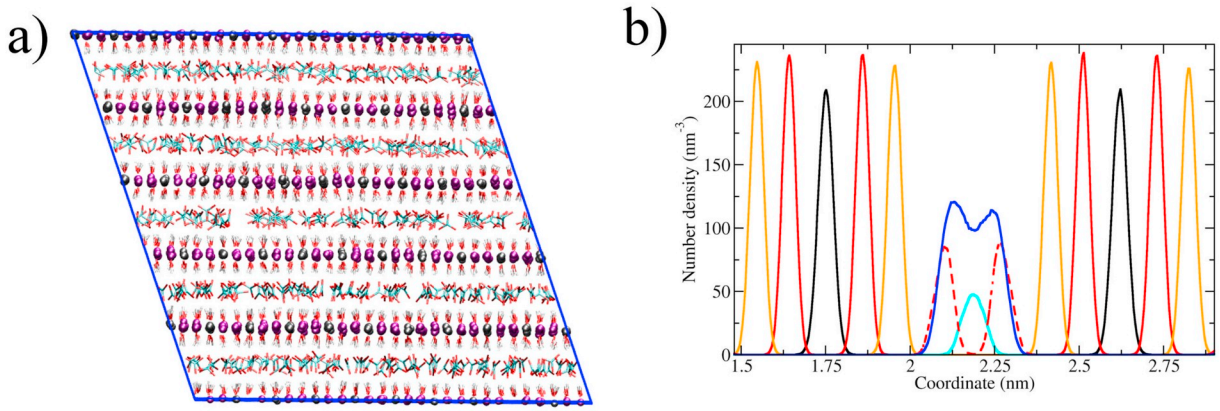

Fig. 9. a) Simulation snapshot attained after 20 ns of simulation time and b) the density profile obtained along the axis normal to the metal layer in the ZII system. The colour code is the same as in Fig. 8a but nitrogen atoms in cyan and water molecules were removed for clarity in a). (For interpretation of the references to colour in this figure legend, the reader is referred to the web version of this article.)

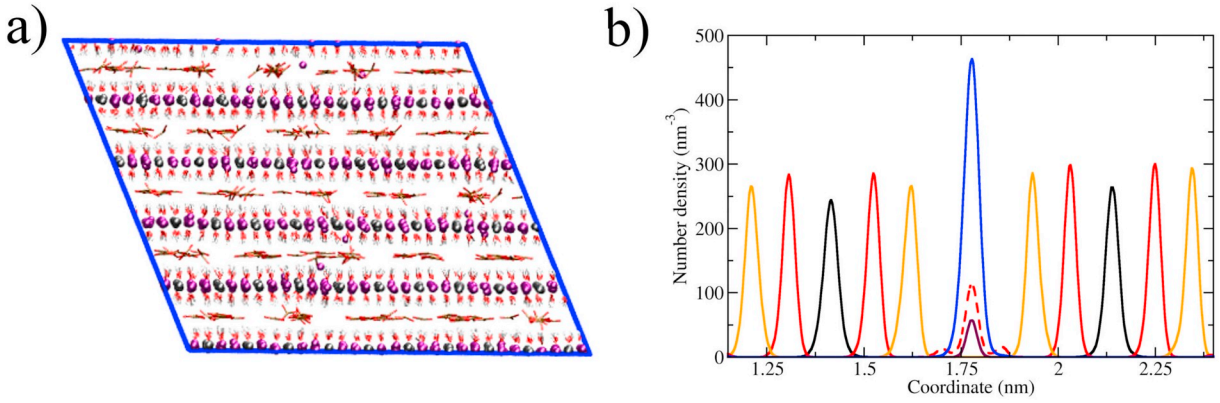

Fig. 10. a) Simulation snapshot attained after 20 ns of simulation time and b) the density profile obtained along the axis normal to the metal layer in the ZIII system. The colour code is the same as in Fig. 8a but carbon atoms in ochre and the water molecules were removed for clarity in a).

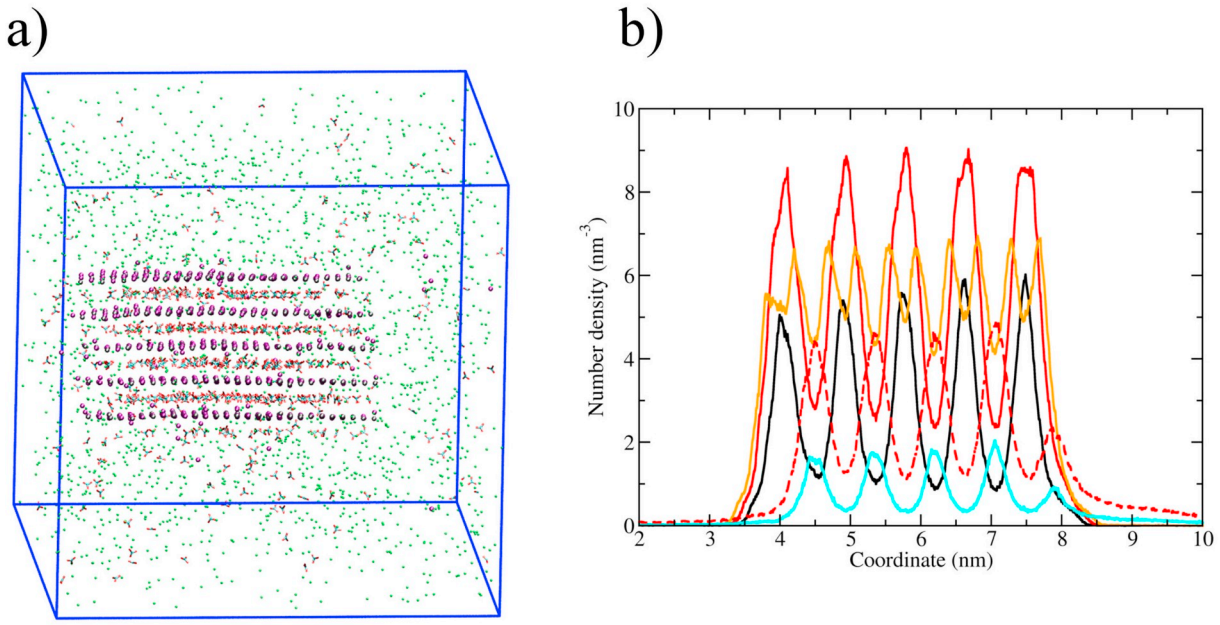

Fig. 11. a) Simulation snapshot obtained after 20 ns of simulation time showing the stability of the ZII system well surrounded by a corrosive sodium chloride water solution. b) density profile along the axis normal to the metal plane. The colour code is the same as in Fig. 9 but chloride anions are in green. The water molecules and sodium anions were removed for clarity. The water in the density profiles of water and the NaCl were removed to focus in the ZII profile. The average interlayer distance obtained by averaging the distances between the metal layer maxima in the density profile is 8.9 Å, close to the experimental value 8.8 Å as well as to the computed XRD 8.94 Å of the system shown in a. (For interpretation of the references to colour in this figure legend, the reader is referred to the web version of this article.)

exchange the nitrate anions by chlorides as well as the proper hydration of each layer independently. However, this process is only partially captured by the present NpT simulations because the ion exchange is a slow process and, hence, much longer simulations times are needed to analyse it in detail. Such simulations are outside the scope of the present work and will be treated in a separate study. Previous approaches were limited in this respect since the number of water molecules inside each interlayer distance must be adjusted prior to the MD simulation.

The XRD profile for the MD simulation is compared in Fig. S9 with the experimental counterpart synthesized in this work. Remarkably, the average distance obtained in the XRD pattern, 8.9 Å, is very close to the MD (8.70 Å) and experimental (8.80 Å) interlayer distances of the ZII system as can be seen in Table 6.

Moreover, besides the model showing the anion exchange ability of the LDH, it also shows the dissolution equilibrium of the metallic atoms in water, as verified in previous experimental works (Galvão et al., 2016). The extent of this equilibrium is enhanced by border effects of the material, since an experimental sample (Galvão et al., 2016) can be constituted of 3D hexagonal plates of (400–1000) nm × (400–1000) nm × (20–40) nm, and in the model depicted in Fig. 11, the material possesses smaller dimensions, 5 nm × 5 nm × 5 nm. However, the metal dissolution found in the simulations is quite negligible in percentage of the total of the metallic species in the simulation box.

From these preliminary simulations with the immersed LDH system, it is clear that the total flexibility of the present model allows to deal with the essential physico-chemical characteristics of LDH materials, which is very encouraging for further computational studies in the field.

5. Conclusions

In this work, a computer simulation model for magnesium and zinc aluminium based LDH materials has been developed to study the role of different intercalated anions in the basal space. Firstly, the Mg_2Al LDH system with Cl^-, NO_3^- or CO_3^{2-} anions (MI-III) has been chosen to validate the computer simulation framework. For this purpose, the computed XRD interlayer distances of each MD system were compared with computational and experimental studies found in the literature. The results were in reasonable agreement to those found in the literature, demonstrating that our MD simulations maintain the expected structure reproducing very well the experimental results. The MD simulations carried in this work showed that on going from one to two water molecules per chloride anion leads to an increase of the interlayer distance by more than one angstrom, together with strong bending of the metal hydroxide layers. In fact, our LDH structures provides a valuable reference to shed light into some dissimilarities found in the literature since the amount of water dramatically modifies the basal space. The computed X-ray patterns displayed for each system can be used as a reference since the number of water molecules per anion in the computed samples is well known.

The density profiles in the normal direction to the metal layer plane were used to study the MD structure obtained in this work, offering a remarkable perspective of the LDH structure. For instance, the distribution and orientation of the anion species in the basal space and how they change with the nature of the anion. Bearing this in mind, the behaviour of two structurally similar but differently charged anions, namely NO_3^- and CO_3^{2-}, in the galleries of Mg_2Al and Zn_2Al LDH were compared. The materials with nitrate anions showed larger interlayer distances than those with carbonate because less anions are needed in the latter to compensate the positive charge of the metal hydroxide layers. As a result of the larger charge density in carbonate than in nitrate anions, the molecular plane of the NO_3^- anions is not coplanar with the planes of the metal hydroxide layers while an opposite behaviour is found for CO_3^{2-} anions.

Some other important conclusions could be extracted from the computational work; the interaction between the partial charges involved in the LDH structure with the partial charge of the intercalated anions mainly maintain the interlayer conformation. The use of the partial charges provided by CLAYFF induced the dissolution of some metal atoms in the basal space, according to some previous computational studies. In these studies, the calculation of new sets partial charges helped to circumvent this issue, however, this procedure reduced the generalisation of the MD model. Conversely, the procedure followed in this work allows the use of the same partial charges regardless of the nature of anionic species. Thus, the approach presented in this study provides a straightforward strategy to perform computer simulations in Mg_2Al and Zn_2Al under a unique model (same LJ parameters and partial charges in the LDH) independently of the intercalated anion used. Most importantly, our approach opens the door to MD simulations with portions of LDH systems immersed in aqueous solutions. Therefore, it can be explored the LDH behaviour under different conditions taking into account the natural hydration and ions exchange observed in experiments.

Supplementary data to this article can be found online at https://doi.org/10.1016/j.clay.2018.06.037.

Acknowledgements

This work was developed in the scope of project CICECO – Aveiro Institute of Materials, POCI-01-0145-FEDER-007679 (Ref. FCT UID/CTM/50011/2013), financed by national funds through the FCT/MEC and when applicable co-financed by FEDER under the PT2020 Partnership Agreement, and in the framework of project SELMAP2020-PTDC/QEQ-QFI/4719/2014, funded by Project 3599 - Promover a Produção Científica e Desenvolvimento Tecnológico e a Constituição de Redes Temáticas (3599-PPCDT) and FEDER funds through COMPETE 2020, Programa Operacional Competitividade e Internacionalização (POCI). The authors also thank financial support from FCT (Programa Investigador FCT). JT thanks FCT for the research grant IF/00347/2013.

References

Abraham, M.J., Murtola, T., Schulz, R., Páll, S., Smith, J.C., Hess, B., Lindahl, E., 2015. GROMACS: high performance molecular simulations through multi-level parallelism from laptops to supercomputers. SoftwareX 1–2, 19–25. https://doi.org/10.1016/j.softx.2015.06.001.

Ay, A.N., Zümreoglu-Karan, B., Mafra, L., 2009. A simple Mechanochemical route to layered double hydroxides: synthesis of Hydrotalcite-like Mg-Al-NO 3 -LDH by manual grinding in a mortar. Z. Anorg. Allg. Chem. 635 (9–10), 1470–1475. https://doi.org/10.1002/zaac.200801287.

Bellotto, M., Rebours, B., Clause, O., Lynch, J., Bazin, D., Elkaïm, E., 1996. A reexamination of hydrotalcite crystal chemistry. J. Phys. Chem. 100 (20), 8527–8534. https://doi.org/10.1021/jp960039j.

Berendsen, H.J.C., Postma, J.P.M., van Gunsteren, W.F., Dinola, A., Haak, J.R., 1984. Molecular dynamics with coupling to an external bath. J. Chem. Phys. 81 (8), 3684–3690. https://doi.org/10.1063/1.448118.

Berendsen, H.J.C., Grigera, J.R., Straatsma, T.P., 1987. The missing term in effective pair potentials. J. Phys. Chem. 91 (24), 6269–6271. https://doi.org/10.1021/j100308a038.

Boclair, J.W., Braterman, P.S., Brister, B.D., Yarberry, F., 1999. Layer − anion interactions in magnesium aluminum layered double hydroxides intercalated with Cobalticyanide and Nitroprusside. Chem. Mater. 11 (8), 2199–2204. https://doi.org/10.1021/cm990148l.

Bravo-Suárez, J.J., Páez-Mozo, E.A., Oyama, S.T., 2004. Review of the synthesis of layered double hydroxides: a thermodynamic approach. Quim Nova 27 (4). https://doi.org/10.1590/S0100-40422004000400015.

Bussi G., Donadio D., Parrinello M., 2007. Canonical sampling through velocity rescaling. J. Chem. Phys. 126 (1). https://doi.org/10.1063/1.2408420. (014101).

Cadena, C., Maginn, E.J., 2006. Molecular simulation study of some Thermophysical and transport properties of Triazolium-based ionic liquids. J. Phys. Chem. B 110 (36), 18026–18039. https://doi.org/10.1021/jp0629036.

Carneiro, J., Caetano, A.F., Kuznetsova, A., Maia, F., Salak, A.N., Tedim, J., Scharnagl, N., Zheludkevich, M.L., Ferreira, M.G.S., 2015. Polyelectrolyte-modified layered double hydroxide nanocontainers as vehicles for combined inhibitors. RSC Adv. 5 (50), 39916–39929. https://doi.org/10.1039/C5RA03741G.

Costa, D.G., Rocha, A.B., Diniz, R., Souza, W.F., Chiaro, S.S.X., Leitão, A.A., 2010. Structural model proposition and thermodynamic and vibrational analysis of Hydrotalcite-like compounds by DFT calculations. J. Phys. Chem. C 114 (33), 14133–14140. https://doi.org/10.1021/jp1033646.

Costa, D.G., Rocha, A.B., Souza, W.F., Chiaro, S.S.X., Leitão, A.A., 2012. Comparative structural, thermodynamic and electronic analyses of ZnAlAn − hydrotalcite-like

compounds (An − Cl − , F − , Br − , OH − , CO32 − or NO3 −): an ab initio study. Appl. Clay Sci. 56, 16–22. https://doi.org/10.1016/j.clay.2011.11.014.
Cunha, V.R.R., de Souza, R.B., da Fonseca Martins, A.M.C.R.P., Koh, I.H.J., Constantino, V.R.L., 2016. Accessing the biocompatibility of layered double hydroxide by intramuscular implantation: histological and microcirculation evaluation. Sci. Rep. 6 (1), 30547. https://doi.org/10.1038/srep30547.
Cygan, R.T., Liang, J.-J., Kalinichev, A.G., 2004. Molecular models of hydroxide, oxyhydroxide, and clay phases and the development of a general force field. J. Phys. Chem. B 108 (4), 1255–1266. https://doi.org/10.1021/jp0363287.
Cygan, R.T., Greathouse, J.A., Heinz, H., Kalinichev, A.G., 2009. Molecular models and simulations of layered materials. J. Mater. Chem. 19 (17), 2470. https://doi.org/10.1039/b819076c.
Dauber-Osguthorpe, P., Roberts, V.A., Osguthorpe, D.J., Wolff, J., Genest, M., Hagler, A.T., 1988. Structure and energetics of ligand binding to proteins:Escherichia coli dihydrofolate reductase-trimethoprim, a drug-receptor system. Proteins Struct. Funct. Genet. 4 (1), 31–47. https://doi.org/10.1002/prot.340040106.
Ennadi, A., Legrouri, A., De Roy, A., Besse, J.P., 2000. X-ray diffraction pattern simulation for thermally treated [Zn–Al–Cl] layered double hydroxide. J. Solid State Chem. 152 (2), 568–572. https://doi.org/10.1006/jssc.2000.8740.
Galvão, T.L.P., Neves, C.S., Caetano, A.P.F., Maia, F., Mata, D., Malheiro, E., Ferreira, M.J., Bastos, A.C., Salak, A.N., Gomes, J.R.B., et al., 2016. Control of crystallite and particle size in the synthesis of layered double hydroxides: macromolecular insights and a complementary modeling tool. J. Colloid Interface Sci. 468, 86–94. https://doi.org/10.1016/j.jcis.2016.01.038.
Galvão, T.L.P., Neves, C.S., Zheludkevich, M.L., Gomes, J.R.B., Tedim, J., Ferreira, M.G.S., 2017. How density functional theory surface energies may explain the morphology of particles, nanosheets, and conversion films based on layered double hydroxides. J. Phys. Chem. C 121 (4), 2211–2220. https://doi.org/10.1021/acs.jpcc.6b10860.
Giannozzi, P., Baroni, S., Bonini, N., Calandra, M., Car, R., Cavazzoni, C., Ceresoli, D., Chiarotti, G.L., Cococcioni, M., Dabo, I., et al., 2009. QUANTUM ESPRESSO: a modular and open-source software project for quantum simulations of materials. J. Phys. Condens. Matter 21 (39), 395502. https://doi.org/10.1088/0953-8984/21/39/395502.
Groom, C.R., Bruno, I.J., Lightfoot, M.P., Ward, S.C., 2016. The Cambridge structural database. Acta Crystallogr. Sect. B Struct. Sci. Cryst. Eng. Mater. 72 (2), 171–179. https://doi.org/10.1107/S2052520616003954.
Hess, B., Bekker, H., Berendsen, H.J.C., Fraaije, J.G.E.M., 1997. LINCS: a linear constraint solver for molecular simulations. J. Comput. Chem. 18 (12), 1463–1472. https://doi.org/10.1002/(SICI)1096-987X(199709)18:12<1463::AID-JCC4>3.0.CO;2-H.
Hockney, R., Goel, S., Eastwood, J., 1974. Quiet high-resolution computer models of a plasma. J. Comput. Phys. 14 (2), 148–158. https://doi.org/10.1016/0021-9991(74)90010-2.
Hoover, W.G., 1985. Canonical dynamics: equilibrium phase-space distributions. Phys. Rev. A 31 (3), 1695–1697. https://doi.org/10.1103/PhysRevA.31.1695.
Israëli, Y., Taviot-Guého, C., Besse, J.-P., Morel, J.-P., Morel-Desrosiers, N., 2000. Thermodynamics of anion exchange on a chloride-intercalated zinc–aluminum layered double hydroxide: a microcalorimetric study. J. Chem. Soc. Dalton Trans. 5, 791–796. https://doi.org/10.1039/a906346c.
Káfuňková, E., Taviot-Guého, C., Bezdička, P., Klementová, M., Kovář, P., Kubát, P., Mosinger, J., Pospíšil, M., Lang, K., 2010. Porphyrins intercalated in Zn/Al and Mg/Al layered double hydroxides: properties and structural arrangement. Chem. Mater. 22 (8), 2481–2490. https://doi.org/10.1021/cm903125v.
Kim, N., Kim, Y., Tsotsis, T.T., Sahimi, M., 2005. Atomistic simulation of nanoporous layered double hydroxide materials and their properties I. Structural modeling. J. Chem. Phys. 122 (21), 214713. https://doi.org/10.1063/1.1902945.
Kim, N., Harale, A., Tsotsis, T.T., Sahimi, M., 2007. Atomistic simulation of nanoporous layered double hydroxide materials and their properties. II. Adsorption and diffusion. J. Chem. Phys. 127 (22), 224701. https://doi.org/10.1063/1.2799985.
Kresse, G., Furthmüller, J., 1996a. Efficiency of ab-initio total energy calculations for metals and semiconductors using a plane-wave basis set. Comput. Mater. Sci. 6 (1), 15–50.
Kresse, G., Furthmüller, J., 1996b. Efficient iterative schemes for ab initio total-energy calculations using a plane-wave basis set. Phys. Rev. B 11169–11186.
Kresse, G., Hafner, J., 1993. Ab initio molecular dynamics for liquid metals. Phys. Rev. B 47 (1), 558–561.
Kresse, G., Joubert, D., 1999. From ultrasoft pseudopotentials to the projector augmented-wave method. Phys. Rev. B 59 (3), 1758–1775. https://doi.org/10.1103/PhysRevB.59.1758.
Krivovichev, S.V., Yakovenchuk, V.N., Zhitova, E.S., Zolotarev, A.A., Pakhomovsky, Y.A., Ivanyuk, G.Y., 2010. Crystal chemistry of natural layered double hydroxides. 2. Quintinite-1M: first evidence of a monoclinic polytype in M2 + − M3 + layered double hydroxides. Mineral. Mag. 74 (5), 833–840. https://doi.org/10.1180/minmag.2010.074.5.833.
Latterini, L., Nocchetti, M., Aloisi, G.G., Costantino, U., De Schryver, F.C., Elisei, F., 2007. Structural, Photophysical, and photochemical characterization of 9-Anthracenecarboxylate − Hydrotalcite Nanocomposites: evidence of a reversible light-driven reaction. Langmuir 23 (24), 12337–12343. https://doi.org/10.1021/la7014989.
Li, L., Gu, Z., Gu, W., Liu, J., Xu, Z.P., 2016. Efficient drug delivery using SiO 2 -layered double hydroxide nanocomposites. J. Colloid Interface Sci. 470, 47–55. https://doi.org/10.1016/j.jcis.2016.02.042.
Limas, N.G., Manz, T.A., 2016. Introducing DDEC6 atomic population analysis: part 2. Computed results for a wide range of periodic and nonperiodic materials. RSC Adv. 6 (51), 45727–45747. https://doi.org/10.1039/C6RA05507A.
Lombardo, G.M., Pappalardo, G.C., Punzo, F., Costantino, F., Costantino, U., Sisani, M., 2005. A novel integrated X-ray powder diffraction (XRPD) and molecular dynamics (MD) approach for modelling mixed-metal (Zn, Al) layered double hydroxides (LDHs). Eur. J. Inorg. Chem. 2005 (24), 5026–5034. https://doi.org/10.1002/ejic.200500666.
Lu, Z., Qian, L., Tian, Y., Li, Y., Sun, X., Duan, X., 2016a. Ternary NiFeMn layered double hydroxides as highly-efficient oxygen evolution catalysts. Chem. Commun. 52 (5), 908–911. https://doi.org/10.1039/C5CC08845C.
Lu, Y., Jiang, B., Fang, L., Ling, F., Gao, J., Wu, F., Zhang, X., 2016b. High performance NiFe layered double hydroxide for methyl orange dye and Cr(VI) adsorption. Chemosphere 152, 415–422. https://doi.org/10.1016/j.chemosphere.2016.03.015.
Lv, K., Kang, H., Zhang, H., Yuan, S., 2012. Molecular simulation studies for intercalation of photoactive dyes into layered double hydroxide. Colloids Surf. A Physicochem. Eng. Asp. 402, 108–116. https://doi.org/10.1016/j.colsurfa.2012.03.032.
Mahjoubi, F.Z., Khalidi, A., Abdennouri, M., Barka, N., 2017. Zn–Al layered double hydroxides intercalated with carbonate, nitrate, chloride and sulphate ions: synthesis, characterisation and dye removal properties. J. Taibah Univ. Sci. 11 (1), 90–100. https://doi.org/10.1016/j.jtusci.2015.10.007.
Makaremi, M., Jordan, K.D., Guthrie, G.D., Myshakin, E.M., 2015. Multiphase Monte Carlo and Molecular dynamics simulations of water and CO 2 intercalation in Montmorillonite and Beidellite. J. Phys. Chem. C 119 (27), 15112–15124. https://doi.org/10.1021/acs.jpcc.5b01754.
Manz, T.A., Limas, N.G., 2016. Introducing DDEC6 atomic population analysis: part 1. Charge partitioning theory and methodology. RSC Adv. 6 (53), 47771–47801. https://doi.org/10.1039/C6RA04656H.
Maruyama, S.A., Tavares, S.R., Leitão, A.A., Wypych, F., 2016. Intercalation of indigo carmine anions into zinc hydroxide salt: a novel alternative blue pigment. Dyes Pigments 128, 158–164. https://doi.org/10.1016/j.dyepig.2016.01.022.
Marzari, N., Vanderbilt, D., De Vita, A., Payne, M.C., 1999. Thermal contraction and disordering of the Al(110) surface. Phys. Rev. Lett. 82 (16), 3296–3299. https://doi.org/10.1103/PhysRevLett.82.3296.
Miyata, S., 1983. Anion-exchange properties of Hydrotalcite-like compounds. Clay Clay Miner. 31 (4), 305–311. https://doi.org/10.1346/CCMN.1983.0310409.
Monkhorst, H.J., Pack, J.D., 1976. Special points for Brillouin-zone integrations. Phys. Rev. B 13 (12), 5188–5192. https://doi.org/10.1103/PhysRevB.13.5188.
Nosé, S., 1984. A molecular dynamics method for simulations in the canonical ensemble. Mol. Phys. 52 (2), 255–268. https://doi.org/10.1080/00268978400101201.
Parrinello, M., Rahman, A., 1981. Polymorphic transitions in single crystals: a new molecular dynamics method. J. Appl. Phys. 52 (12), 7182–7190. https://doi.org/10.1063/1.328693.
Perdew, J.P., Burke, K., Ernzerhof, M., 1996. Generalized gradient approximation made simple. Phys. Rev. Lett. 77 (18), 3865–3868. https://doi.org/10.1103/PhysRevLett.77.3865.
Poznyak, S.K., Tedim, J., Rodrigues, L.M., Salak, A.N., Zheludkevich, M.L., Dick, L.F.P., Ferreira, M.G.S., 2009. Novel inorganic host layered double hydroxides intercalated with guest organic inhibitors for anticorrosion applications. ACS Appl. Mater. Interfaces 1 (10), 2353–2362. https://doi.org/10.1021/am900495r.
Rad, F.A., Rezvani, Z., Khodam, F., 2016. Molecular design confirmation for proposition of improved photophysical properties in a dye-intercalated layered double hydroxides. RSC Adv. 6 (14), 11193–11203. https://doi.org/10.1039/C5RA19209A.
Radha, A.V., Kamath, P.V., Shivakumara, C., 2007. Order and disorder among the layered double hydroxides: combined Rietveld and DIFFaX approach. Acta Crystallogr. Sect. B Struct. Sci. 63 (2), 243–250. https://doi.org/10.1107/S010876810700122X.
Richetta, M., Medaglia, PG., Mattoccia, A., Varone, A., Pizzoferrato, R., 2017. Layered double hydroxides: tailoring interlamellar nanospace for a vast field of applications. J. Mater. Sci. Eng. 6 (360), 1–9. https://doi.org/10.4172/2169-0022.1000360.
Schmid, N., Eichenberger, A.P., Choutko, A., Riniker, S., Winger, M., Mark, A.E., van Gunsteren, W.F., 2011. Definition and testing of the GROMOS force-field versions 54A7 and 54B7. Eur. Biophys. J. 40 (7), 843–856. https://doi.org/10.1007/s00249-011-0700-9.
Senapati, S., Thakur, R., Verma, S.P., Duggal, S., Mishra, D.P., Das, P., Shripathi, T., Kumar, M., Rana, D., Maiti, P., 2016. Layered double hydroxides as effective carrier for anticancer drugs and tailoring of release rate through interlayer anions. J. Control. Release 224, 186–198. https://doi.org/10.1016/j.jconrel.2016.01.016.
Serdechnova, M., Salak, A.N., Barbosa, F.S., Vieira, D.E.L., Tedim, J., Zheludkevich, M.L., Ferreira, M.G.S., 2016. Interlayer intercalation and arrangement of 2-mercaptobenzothiazolate and 1,2,3-benzotriazolate anions in layered double hydroxides: in situ X-ray diffraction study. J. Solid State Chem. 233, 158–165. https://doi.org/10.1016/j.jssc.2015.10.023.
Smith, D.E., Dang, L.X., 1994. Computer simulations of NaCl association in polarizable water. J. Chem. Phys. 100 (5), 3757–3766. https://doi.org/10.1063/1.466363.
Sun, Z., Jin, L., Shi, W., Wei, M., Duan, X., 2010. Preparation of an anion dye intercalated into layered double hydroxides and its controllable luminescence properties. Chem. Eng. J. 161 (1–2), 293–300. https://doi.org/10.1016/j.cej.2010.04.031.
Tedim, J., Zheludkevich, M.L., Salak, A.N., Lisenkov, A., Ferreira, M.G.S., 2011. Nanostructured LDH-container layer with active protection functionality. J. Mater. Chem. 21 (39), 15464. https://doi.org/10.1039/c1jm12463c.
Tedim, J., Kuznetsova, A., Salak, A.N., Montemor, F., Snihirova, D., Pilz, M., Zheludkevich, M.L., Ferreira, M.G.S., 2012. Zn–Al layered double hydroxides as chloride nanotraps in active protective coatings. Corros. Sci. 55, 1–4. https://doi.org/10.1016/j.corsci.2011.10.003.
Thyveetil, M.-A., Coveney, P.V., Suter, J.L., Greenwell, H.C., 2007. Emergence of Undulations and Determination of Materials Properties in Large-Scale Molecular Dynamics Simulation of Layered Double Hydroxides. https://doi.org/10.1021/CM070923U.
Thyveetil, M.-A., Coveney, P.V., Greenwell, H.C., Suter, J.L., 2008. Role of host layer flexibility in DNA guest intercalation revealed by computer simulation of layered

nanomaterials. J. Am. Chem. Soc. 130 (37), 12485–12495. https://doi.org/10.1021/ja8037068.
Tsukanov, A.A., Psakhie, S.G., 2016. Energy and structure of bonds in the interaction of organic anions with layered double hydroxide nanosheets: a molecular dynamics study. Sci. Rep. 6 (1), 19986. https://doi.org/10.1038/srep19986.
Vanderbilt, D., 1990. Soft self-consistent pseudopotentials in a generalized eigenvalue formalism. Phys. Rev. B 41, 7892–7895. https://doi.org/10.1103/PhysRevB.41.7892.
Velu, S., Ramkumar, V., Narayanan, A., Swamy, C.S., 1997. Effect of interlayer anions on the physicochemical properties of zinc–aluminium hydrotalcite-like compounds. J. Mater. Sci. 32 (4), 957–964. https://doi.org/10.1023/A:1018561918863.
Wang, S.-L., Wang, P.-C., 2007. In situ XRD and ATR-FTIR study on the molecular orientation of interlayer nitrate in mg/Al-layered double hydroxides in water. Colloids Surf. A Physicochem. Eng. Asp. 292 (2–3), 131–138. https://doi.org/10.1016/j.colsurfa.2006.06.014.
Wang, J., Kalinichev, A.G., Kirkpatrick, R.J., Hou, X., 2001. Molecular modeling of the structure and energetics of Hydrotalcite hydration. Chem. Mater. 13 (1), 145–150. https://doi.org/10.1021/cm000441h.
Wang, S., Liu, C., Wang, M., Chuang, Y., Chiang, P., 2009. Arsenate adsorption by Mg/Al–NO3 layered double hydroxides with varying the Mg/Al ratio. Appl. Clay Sci. 43 (1), 79–85. https://doi.org/10.1016/j.clay.2008.07.005.
Yan, Z., Zhu, B., Yu, J., Xu, Z., 2016. Effect of calcination on adsorption performance of Mg–Al layered double hydroxide prepared by a water-in-oil microemulsion method. RSC Adv. 6 (55), 50128–50137. https://doi.org/10.1039/C6RA05253C.
Yokoi, T., Hara, M., Seki, T., Terasaka, S., Kamitakahara, M., Matsubara, H., 2016. Synthesis of layered double hydroxide coatings with an oriented structure and controllable thickness on aluminium substrates. CrystEngComm 18 (7), 1207–1214. https://doi.org/10.1039/C5CE02292D.
Zheludkevich, M.L., Tedim, J., Ferreira, M.G.S., 2012. “Smart” coatings for active corrosion protection based on multi-functional micro and nanocontainers. Electrochim. Acta 82, 314–323. https://doi.org/10.1016/j.electacta.2012.04.095.